Uncovering the Local Magnesium Environment in the Metal–Organic Framework Mg$_2$(dobpdc) Using ^{25}Mg NMR Spectroscopy

Jun Xu,[†,]* E.S. (Merijn) Blaakmeer,[ǁ] Andrew S. Lipton,[ʃʃ] Thomas M. McDonald,[‡] Yifei Michelle Liu,[†] Berend Smit,[†,§] Jeffrey R. Long,[†,‡,ϕ] Arno P.M. Kentgens,[ǁ] Jeffrey A. Reimer.[ϕ,†]

[†]Department of Chemical and Biomolecular Engineering and [‡]Department of Chemistry, University of California, Berkeley, California 94720, United States

[ǁ]Radboud University, Institute for Molecules and Materials, Heyendaalsweg 135, 6525 AJ Nijmegen, The Netherlands

[ʃʃ]Environmental Molecular Sciences Laboratory, Pacific Northwest National Laboratory, 902 Battelle Boulevard, Richland, Washington 99354, United States

[§]Laboratory of Molecular Simulation, Institut des Sciences et Ingénierie Chimiques, Valais Ecole Polytechnique Fédérale de Lausanne (EPFL), Rue de l'Industrie 17, CH-1951 Sion, Switzerland

[ϕ]Materials Sciences Division, Lawrence Berkeley National Laboratory, Berkeley, California 94720, United States

*Email: qidongxujun@gmail.com.

1

Abstract: The incorporation of *N,N′*-dimethylethylenediamine into an expanded MOF-74 framework has yielded a material (mmen-Mg_2(dobpdc)) exhibiting "step-shaped" CO_2 adsorption isotherms. The coordination of mmen at the Mg open metal center is essential for the unique cooperative adsorption mechanism elucidated for this material. Despite its importance for carbon capture, there is as yet no experimental structure determination available for the underlying metal–organic framework Mg_2(dobpdc). Our ^{25}Mg solid-state NMR data unravel the local Mg environments in several Mg_2(dobpdc) samples, unambiguously confirming the formation of five-coordinate Mg centers in the activated material and six-coordinate Mg centers in the solvent- or diamine-loaded samples, such as mmen-Mg_2(dobpdc). A fraction of Mg centers is local disordered due to the framework deformation accompanied by the guest distributions and dynamics.

Introduction

Climate change arising from increasing atmospheric CO_2 levels has become a global concern.[1,2] Capturing CO_2 from the flue gas of fossil fuel-fired power plants has therefore attracted considerable attention in recent years.[3-6] Numerous materials have been developed for removal of CO_2 from flue gas streams, including zeolites,[7] metal−organic frameworks (MOFs),[8] covalent organic frameworks,[9] and many others.[6] Particular attention has been paid to MOFs with coordinatively-unsaturated metal centers such as MOF-74, because they can exhibit a large CO_2 uptake and a high selectivity due to the strong interaction between metal and CO_2.[10-13] The recent incorporation of mmen (N,N'-dimethylethylenediamine) into an expanded MOF-74 framework yielded the material mmen-Mg$_2$(dobpdc) (dobpdc^{4-} = 4,4′-dioxido-3,3′-biphenyldicarboxylate) exhibiting "step-shaped" CO_2 adsorption isotherms that facilitate temperature- or pressure-swing adsorption processes.[14] The coordination of mmen at the Mg centers exposed on the surface of the MOF channels is essential for the proposed adsorption mechanism.[14,15] Despite the importance of mmen-Mg$_2$(dobpdc) as a carbon capture material, however, there is no experimentally determined structure for the underlying Mg$_2$(dobpdc) MOF, owing to the lack of suitable single crystals and the poor resolution of powder diffraction data obtained thus far. Instead, the structure of Mg$_2$(dobpdc) has been elucidated on the basis of the similarity between its powder X-ray diffraction (XRD) pattern and those of its more crystalline analogues, such as Mn$_2$(dobpdc),[14] or through density functional theory (DFT) calculations.[15] It is noteworthy that even the structure of mmen-Mn$_2$(dobpdc) solved from the low temperature single-crystal XRD data is inaccurate, *e.g.*, yielding abnormally long (> 2 Å) N–H bonds. We are thus motivated to investigate experimentally the structures of the activated Mg$_2$(dobpdc) and the solvent- or mmen-loaded samples utilizing ^{25}Mg

solid-state NMR (SSNMR) spectroscopy, with the ultimate intent of discerning the local Mg environments after activation and guest inclusion.
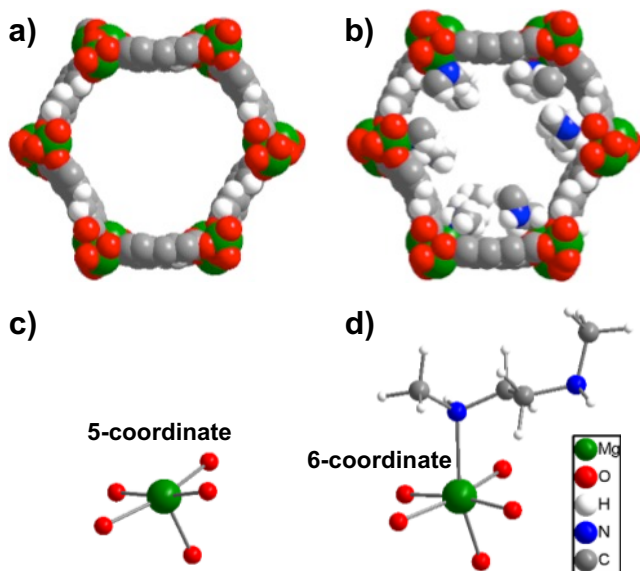

Figure 1. Space-filling models of calculated structures[15] of the activated (a) and mmen-loaded $Mg_2(dobpdc)$ (mmen : Mg = 6 : 6) (b). Ball-and-stick models of the proposed five- (c) and six-coordinate (d) Mg centers.

Figure 1 illustrates calculated structures of the activated and mmen-loaded $Mg_2(dobpdc)$.[15] The framework of $Mg_2(dobpdc)$ consists of interconnecting helical chains of edge-shared MgO_5 units, forming one-dimensional honeycomb channels. These calculations suggest that the local Mg environment changes from five-coordinate in the activated sample to six-coordinate when loaded with guest molecules such as mmen. ^{25}Mg SSNMR spectroscopy is capable of identifying these Mg coordination environments, because the interaction between the nuclear quadrupole moment of ^{25}Mg (spin $I = 5/2$) and the local electric field gradient (EFG) is highly sensitive to the spatial arrangement of neighboring atoms around the ^{25}Mg nucleus.[16-27] Moreover, ^{25}Mg SSNMR spectroscopy can probe the local disorder around Mg centers which are unavailable in diffraction-

based techniques such as XRD. A previous [25]Mg SSNMR study examined several samples of Mg-MOF-74, also known as $Mg_2(dobdc)$ ($dobdc^{4-}$ = 1,4-dioxido-2,5-benzenedicarboxylate), and revealed that the perfect ordering of local Mg environments only exists in water-rich samples, while a local disorder of Mg environments persists in the activated material and most of its guest-loaded forms.[28]

Herein we analyze [25]Mg SSNMR data collected at a high magnetic field of 20.0 T, thereby exploring the local Mg environment in the activated $Mg_2(dobpdc)$ and the solvent- or mmen-loaded samples. The results confirm the formation of five-coordinate Mg centers after activation, as well as identify six-coordinate Mg centers in the guest-loaded samples. Under conditions of fast magic-angle sample spinning, we further probed the nature of local disorder at Mg centers and concluded that the NMR-observed local disorder is due to the guest distributions and dynamics, as supported by DFT calculations and molecular dynamics (MD) simulations.

Experimental and Theoretical Methods

Sample Preparation. The [25]MgO (99.2 atom %, purchased from Cortecnet) was dissolved in excess dilute nitric acid. The resulting [25]$Mg(NO_3)_2$ solution was concentrated at 363 K and then crystallized in an ice bath. The precipitated crystals were purified by recrystallization. The DMF-loaded [25]$Mg_2(dobpdc)$ was synthesized exactly as described previously using the obtained [25]Mg-enriched [25]$Mg(NO_3)_2$ crystals and then stored in DMF.[29] The CH_3OH-loaded [25]$Mg_2(dobpdc)$ was prepared by soaking the DMF-loaded [25]$Mg_2(dobpdc)$ in fresh methanol and then discarding the liquid, repeated three times. The activated [25]Mg-enriched sample was prepared by evacuating the CH_3OH-loaded sample under dynamic vacuum at 523 K for ~ 12 hours. The preparation of the mmen-[25]$Mg_2(dobpdc)$ involved adding mmen solution (in toluene) to the activated [25]$Mg_2(dobpdc)$ in

an argon glove bag and filtering this mixture after 2 days. The mmen-^{25}Mg$_2$(dobpdc) was then heated under dynamic vacuum at 373 K for 4 hours to remove the residual toluene. The H$_2$O-loaded ^{25}Mg$_2$(dobpdc) was prepared by soaking the activated ^{25}Mg$_2$(dobpdc) in H$_2$O for 12 hours and then collecting the solid. The activated and mmen-loaded ^{25}Mg$_2$(dobpdc) were packed into NMR rotors in a glove box. The preparation of natural abundance Mg$_2$(dobpdc) samples was similar to that of the ^{25}Mg-enriched samples but used natural abundance starting materials.

Powder X-Ray Diffraction. Diffraction data were collected with 0.02° steps from 2° to 50° using a Bruker AXS D8 Advance diffractometer equipped with Cu–Kα radiation (λ = 1.5418 Å), a Göbel mirror, a Lynxeye linear position-sensitive director, and mounting the following optics: fixed divergence slit (0.6 mm), receiving slit (3 mm), and secondary beam Soller slits (2.5°). The generator was set at 40 kV and 40 mA. Powder XRD patterns (Figure S1) verify the purity and integrity of ^{25}Mg$_2$(dobpdc) samples.

Solid-State NMR Spectroscopy. Static ^{25}Mg SSNMR experiments were performed at 20.0 T (850 MHz for proton) on an Agilent VNMRS spectrometer at the Environmental Molecular Sciences Laboratory (EMSL), Pacific Northwest National Laboratory (PNNL), using a 4 mm MAS probe (double tuned to ^{1}H/^{25}Mg). Both 90°–τ–180° echo and quadrupolar Carr-Purcell-Meiboom-Gill (QCPMG) experiments were performed.[30,31] The spike separation in QCPMG experiments was 1 kHz. A ^{25}Mg 90° pulse of 6 μs was measured using saturated MgCl$_2$(aq), corresponding to a selective 90° pulse of 2 μs for solid samples. A Double Frequency Sweep (DFS) sequence was integrated into both echo and QCPMG sequences to enhance the signal sensitivity.[32] The DFS parameters were optimized using a ^{25}Mg(HCOO)$_2$· 2H$_2$O sample. The recycle delays were between 10 s and 20 s. Two-Pulse Phase-Modulated (TPPM) ^{1}H decoupling scheme was used in static ^{25}Mg SSNMR experiments.[33] The ^{1}H decoupling field strength is approximately 40 kHz.

Magic-angle spinning (MAS) [25]Mg SSNMR experiments were performed at 20.0 T (850 MHz for proton) on an Agilent VNMRS spectrometer at Radboud University, the Netherlands, using either a 1.6 mm MAS probe (double tuned to ^{1}H/[25]Mg) or a 1.2 mm MAS probe (double tuned to ^{1}H/[25]Mg). Rotor-synchronized 30°–τ–180° echo experiments were performed under 37.5 kHz MAS. A short flip angle of 30° was used to accelerate the relaxation of [25]Mg. The refocusing pulse was still 180° for maximum signal. The [25]Mg 90° pulse was found using saturated $MgCl_2$(aq), corresponding to a RF field strength of 40 kHz. A Sideband-selective Double Frequency Sweep (ssDFS) sequence was integrated into the echo sequence to enhance the signal sensitivity.[34,35] The ssDFS parameters were optimized using the DMF-loaded sample. A recycle delay of 0.3 s was used for all samples. Other delay times including 0.1, 0.5, 0.6, 1 and 10 s were used for selected samples to illustrate the effects of slow relaxation for the perfectly ordered Mg centers.

[25]Mg chemical shifts were referenced to saturated $MgCl_2$(aq) at 0 ppm. Simulations of [25]Mg SSNMR spectra were performed using the dmfit program.[36] A Czjzek distribution was used to simulate the line shape of disordered Mg.[37,38] Magneium-25 SSNMR parameters were first adjusted by observations and then fine-tuned using the auto-fit function of the dmfit program. The errors were estimated by varying the optimum parameters until noticeable change was identified.
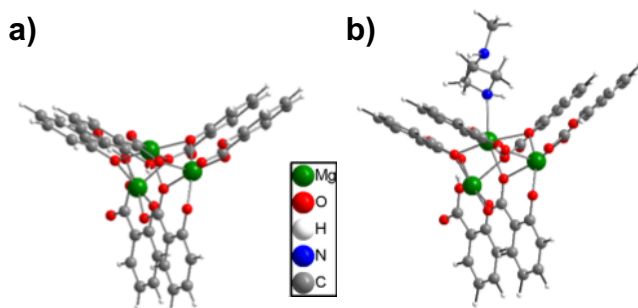

Figure 2. Ball-and-stick models of clusters for DFT calculations: the five-coordinate (a) and six-coordinate (b) Mg centers.

Theoretical Calculations. *Ab initio* density functional theory (DFT) calculations were performed using the NorthWest computational Chemistry (NWChem, version 6.5) software package,[39] which is developed at the EMSL in PNNL, running on the Cascade cluster in EMSL. Magneium-25 isotropic chemical shielding (σ_{iso}), quadrupolar coupling constant (C_Q), and asymmetry parameter (η_Q) were calculated at B3LYP/6-31+G* level using the GIAO method. The periodic structures of the activated and mmen-loaded Mg_2(dobpdc) were taken from the literature (**Figure S2**), which in turn are calculated under periodic boundary conditions.[15] The space group was set to P_1 in their calculations, yielding 6 non-equivalent Mg sites instead of 1 in the proposed space group $P3_221$. As a result, two mmen-loaded Mg_2(dobpdc) structures were calculated: one with all 6 Mg sites covered by mmen and the other with only 1 Mg site (*i.e.*, Mg3) covered by mmen. The model clusters used in NMR calculations were truncated from the above-mentioned periodic structures and terminated with H atoms, which contain three Mg centers and six half-ligands (**Figure 2**). Calculated NMR parameters, including σ_{iso}, V_{ZZ}, and η_Q, were directly read from NMChem output files. The C_Q values were calculated using $C_Q = (eQV_{ZZ})/h$, where e is the electric charge and h is the Planck's constant. Calculated σ_{iso} values were converted to calculated chemical shift (δ_{iso}) values using the following equation: $\delta_{iso} = 613.2 - \sigma_{iso}$ (in ppm), where 613.2 ppm is the calculated σ_{iso} value of $Mg(H_2O)_6^{2+}$ at B3LYP/6-31+G* level. The geometry of $Mg(H_2O)_6^{2+}$ was optimized at MP2/6-31+G* level prior to NMR calculations. The results are shown in **Table S1**.

Molecular Dynamics (MD) simulations of the mmen-Mg_2(dobpdc) were performed using LAMMPS molecular dynamics package (28 June 2014 version)[40] on the Edison cluster of the Department of Energy National Energy Research Scientific Computing Center (NERSC). NPT simulations were run in a triclinic box with periodic boundary conditions and an anisotropic

Parrinello-Rahman barostat, using a timestep of 0.25 fs and a unit cell (taken from the structure in the literature[15], mmen : Mg = 6 : 6) replicated 2 times in the *a* and *b* directions and 4 times in the *c* direction, corresponding to N = 3072 atoms. The simulations used the ReaxFF method introduced in 2001 by van Duin[41] via the user supplied ReaxFF package.[42] Force field parameters for N/C/O/H were taken from those parameterized for CuBTC[43] and parameters for Mg from a set fit to MgH[44] systems.
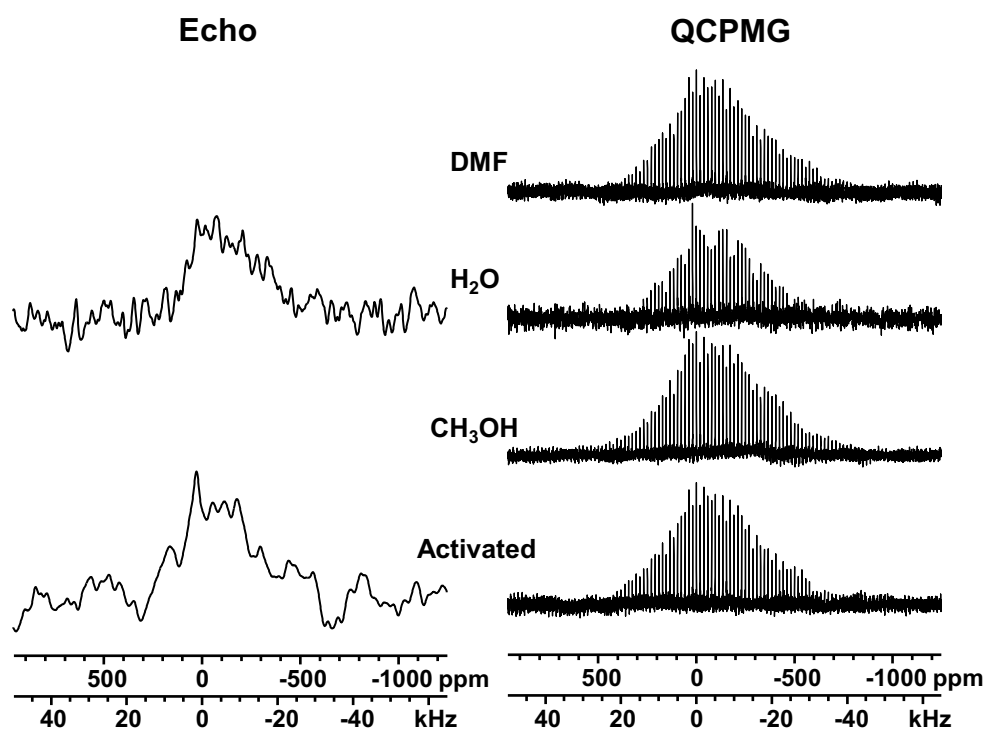
Results and Discussion

Figure 3. Experimental static ^{25}Mg SSNMR spectra of *natural abundance* $Mg_2(dobpdc)$ samples. The recycle delays were between 10 and 20 s.

Static ^{25}Mg SSNMR spectra of *natural abundance* $Mg_2(dobpdc)$ samples were recorded first and shown in Figure 3. Acquisition of these ^{25}Mg SSNMR data are challenging, owing to the relatively large quadrupole moment, small gyromagnetic ratio, and low natural abundance (10.0%)

of ^{25}Mg. These unfavorable nuclear properties result in low sensitivity and broad resonances. This situation is exacerbated by ^{25}Mg concentrations of only 0.21 ^{25}Mg per nm^3 in Mg$_2$(dobpdc) as compared for example to 5.3 for MgO. We addressed these problems by performing SSNMR experiments at high magnetic field[19-28] and using the double frequency sweep (DFS) technique to enhance the sensitivity,[34,45] though the quality of the echo spectra are still very poor. The Quadrupolar Carr-Purcell-Meiboom-Gill (QCPMG) method has been extensively used to acquire the spectrum of insensitive quadrupolar nucleus.[17-26,28,30,46-48] Using the QCPMG method, the overall signal intensity is allocated into sharp spikelets, gaining a boost in signal-to-noise (S/N) ratio at the expense of spectral resolution. The manifold of spikelets resembles the conventional powder pattern observed in the echo experiments. The static QCPMG spectra of the *natural abundance* Mg$_2$(dobpdc) samples, strikingly, all look similar, inconsistent with the proposed (and calculated) large difference of the five-coordinate Mg in the activated sample compared to the six-coordinate Mg in the guest-loaded samples. However, it is known that the broad and weak NMR signals can become "invisible" when the spectral quality is poor, suggesting that an increase in signal (by ^{25}Mg enrichment) would prove benefical.[24,49]
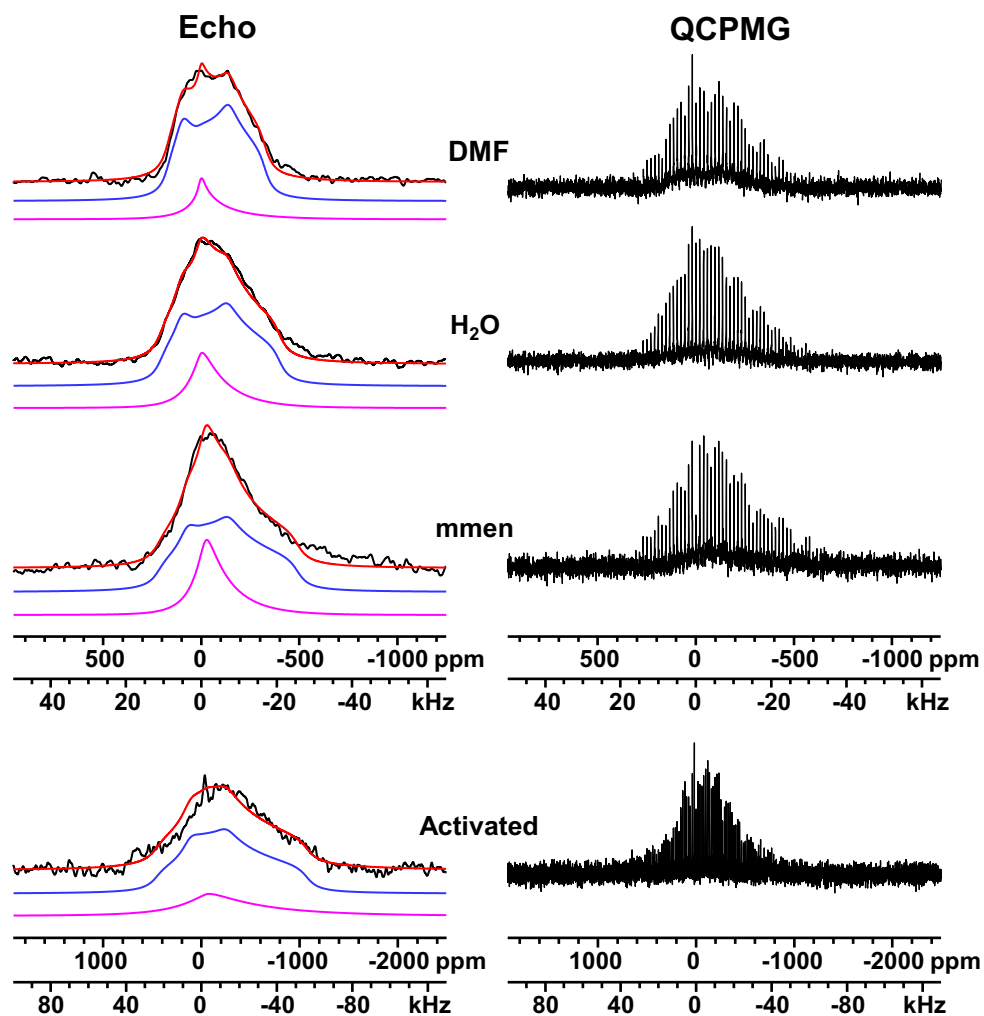
Figure 4. Experimental (black profile) and simulated (red profile) static ^{25}Mg SSNMR spectra of various ^{25}Mg$_2$(dobpdc) samples. The recycle delays were between 10 and 20 s. The simulated spectrum is a summation of powder patterns of the perfectly ordered Mg centers (the blue profile) and the local disordered Mg centers (the purple profile).

^{25}Mg-enriched (99.2% ^{25}Mg) Mg$_2$(dobpdc) samples were then prepared, with their static ^{25}Mg spectra (Figure 4) collected using the same SSNMR methods. After ^{25}Mg-enrichment the quality of the echo spectra are sufficient and thus these spectra were selected for data interpretation. Although the S/N of the QCPMG spectra is higher, they do not exhibit many spectral features and

the baseline is also distorted due to the discard of the first half-echo of the fid.[48] The spectrum of the DMF-loaded sample shows a second-order quadrupolar powder pattern typical of ordered systems, yet with powder pattern discontinuities that are considerably broadened. This broadening becomes more prominent in the spectra of the water- and mmen-loaded samples, yielding featureless and asymmetric powder patterns that are characteristic of Mg centers with significant local disorder. The spectra of three guest-loaded samples spread over a similar frequency range of approximately 20 to −30 kHz (Figure 4). The spectrum of the activated sample, however, looks quite different, exhibiting an even larger span of 40 to −60 kHz. The effect of chemical shift anisotropy (CSA) is negligible in all samples.

The line shape of the ^{25}Mg SSNMR powder pattern is dominated by the interaction between the ^{25}Mg quadrupole moment and the local electric field gradient (EFG). Two EFG parameters are typically reported to describe this interaction: the quadrupolar coupling constant C_Q and the asymmetry parameter η_Q. The C_Q value controls the width of the NMR pattern and is related to the spherical symmetry of the local ground-state electron distribution. A larger C_Q value corresponds to a more distorted local Mg environment away from the perfect spherical symmetry. The η_Q value provides a measure of the axial symmetry of this distribution. The doubling of the activated ^{25}Mg spectral width vis-à-vis those of the guest-loaded samples unambiguously indicates a lower spherical symmetry at Mg centers, consistent with a change from a six-coordinate geometry in the guest-loaded samples to a five-coordinate geometry in the activated sample. The powder pattern discontinuities associated with the activated sample appear to be typical of a second-order quadrupolar pattern, yet our spectral simulations suggest these features may also be associated with local disorder at Mg centers. In order to probe the nature of this disorder further, we employed

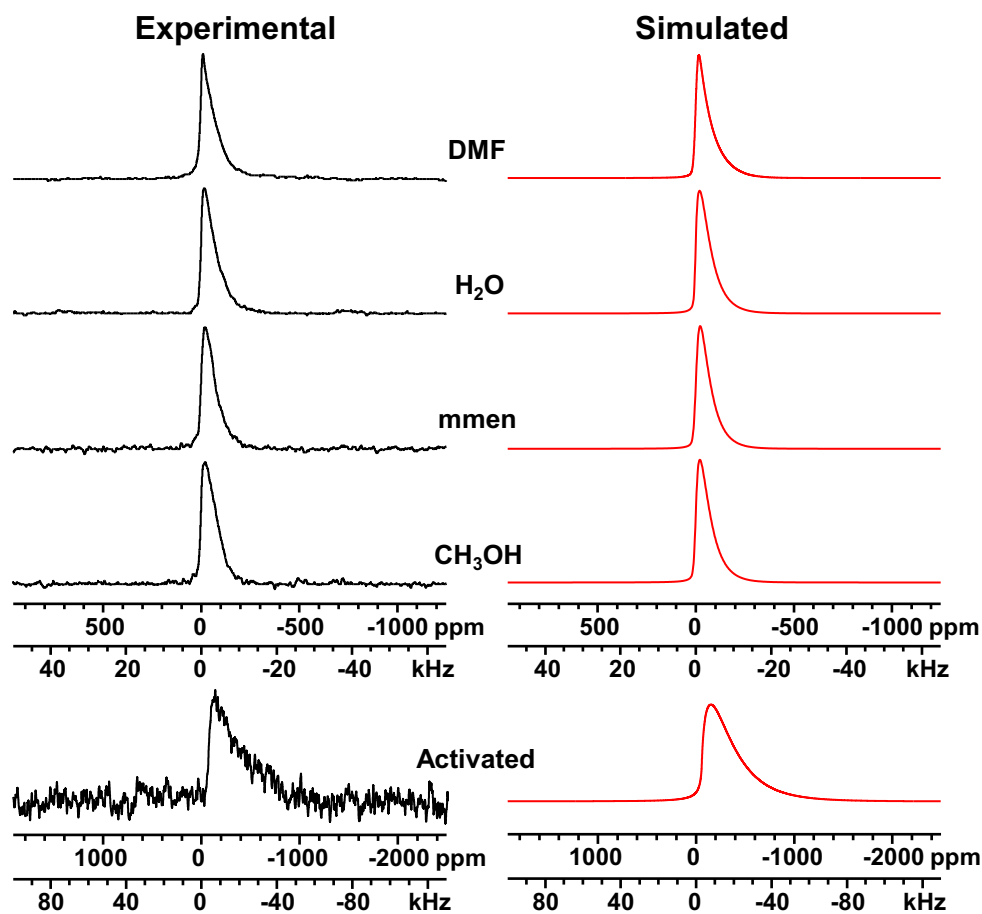relaxation-edited NMR data acquisition as well as magic-angle spinning (MAS) for resolution enhancement.

Figure 5. Experimental (black profile) and simulated (red profile) 37.5 kHz MAS solid echo [25]Mg SSNMR spectra of various [25]Mg[2](dobpdc) samples. The recycle delay was 0.3 s.

Interpretation of [25]Mg SSNMR spectra are often challenging due to the narrow [25]Mg chemical shift range for Mg oxyanion compounds ($\sim \pm 20$ ppm).[22,23] Because the resolution of static SSNMR spectra is often insufficient to resolve multiple Mg sites,[27] magic-angle spinning (MAS) techniques are employed to narrow the powder pattern width to about 1/3 to 1/4 of the static powder pattern width. The method requires, however, a high spinning rate to separate spinning sidebands from the center peak. The data in Figure 4 suggest that a spinning rate of greater than

30 kHz is desirable for MAS experiment of the activated Mg$_2$(dobpdc), which we subsequently achieved using 1.6 mm or 1.2 mm rotors (37.5 kHz spinning rate). The resulting MAS ^{25}Mg solid echo spectra for Mg$_2$(dobpdc) samples at a short recycle delay of 0.3 s are shown in Figure 5.

The MAS spectra of the guest-loaded Mg$_2$(dobpdc) samples exhibit almost identical line shapes, consisting of a narrow asymmetric pattern with a long tail on the low-frequency side. The spectrum of the activated sample shows a similar but significantly broader pattern, consistent with the change in the local spherical symmetry at Mg centers that was observed in the static SSNMR experiments. The observed MAS line shapes are typical of powder patterns for Mg centers with local disorder, *i.e.*, the characteristic powder pattern discontinuities of ordered systems are not present. Such observations indicate that our Mg$_2$(dobpdc) samples likely consist of Mg centers with both perfectly ordered and local disordered environments, and the spin-lattice relaxation of the Mg centers with local disorder must be more efficient than the perfectly ordered Mg centers. The spin-lattice relaxation of ^{25}Mg in solids is usually governed by the strong quadrupolar coupling interaction between the nucleus and the local EFG, which can be effectively accelerated if the local EFG is fluctuated by the thermal motions within the MOF.[50] The details of such motions and their consequence to the local disorder at Mg centers will be discussed later. Shortening the recycle delays under MAS, then, edits the spectra to favor the Mg centers with local disorder. On the basis of the trend of intensity change for both environments, we estimate that the MAS data shown in Figure 5 have less than 6% contribution from the ordered Mg environments if a simplified mono-exponential spin-lattice relaxation behavior is used (Figure S3–S5). This relaxation-edited strategy affords a spectral simulation of the MAS data (Figure 5).

The observed line shapes of MAS spectra can be simulated utilizing the Czjzek distribution of ^{25}Mg EFG parameters.[36-38] In this scheme, the distribution of EFG parameters is described by two

factors: d relates to the number of independent random components of the EFG tensor and C_Q represents the average quadrupolar coupling. A random distribution has a d of 5 while a decreased value of d reflects local geometrical constraints. More details of the Czjzek distribution are shown in Supporting Information. Simulated MAS spectra are shown in Figure 5 and the d and C_Q values for each sample are listed in Table 1. Using the parameters extracted from the MAS experiments, we are able to simulate static spectra as a summation of powder patterns of the local disordered Mg centers and the perfectly ordered Mg centers. These simulation results are shown in Figure 4 and Table 1. It should be mentioned that the relative area between the two Mg local environments obtained in static experiments is only semi-quantitative: firstly, it is unclear if the 10–20 s recycle delays are sufficient for the spin-lattice relaxation of perfectly ordered Mg centers; secondly, it is assumed that the structures of local disordered Mg centers do not change under static and MAS conditions.

Table 1. Experimental ^{25}Mg NMR Parameters.

Sample	Site	d	δ_{iso} (ppm)	C_Q (MHz)	η_Q	Area (%)
DMF	Disordered	3	2	4.8		23
	Ordered		2 ± 2	5.6 ± 0.1	0.40 ± 0.05	77
H_2O	Disordered	5	2	5.0		36
	Ordered		2 ± 2	6.0 ± 0.1	0.50 ± 0.05	64
CH_3OH	Disordered	5	2	4.9		
mmen	Disordered	5	1	4.8		45
	Ordered		1 ± 2	6.3 ± 0.1	0.60 ± 0.05	55
Activated	Disordered	5	9	9.7		22
	Ordered		9 ± 3	8.5 ± 0.2	0.70 ± 0.10	78

The perfectly ordered Mg centers in the guest-loaded samples exhibit C_Q values between 5.6 and 6.3 MHz and η_Q values between 0.4 and 0.6, both of which are comparable to the parameters obtained for the perfectly ordered six-coordinate Mg site in the hydrated Mg$_2$(dobdc).[28] In contrast, a larger C_Q value of 8.5 MHz is observed for the perfectly ordered Mg centers in the activated sample, consistent with the more spherically distorted five-coordinate Mg environment.[18] This assignment is also confirmed by density functional theory (DFT) calculations which yield a C_Q value of 10.4 MHz for the five-coordinate Mg centers in the activated sample and a C_Q value between 4.9 and 8.8 MHz for the six-coordinate Mg centers in the mmen-loaded samples. The significantly higher experimental chemical shift (7–8 ppm) for the five-coordinate Mg centers agrees well with the increase of the calculated chemical shift (11 ppm) when going from the mmen-loaded samples to the activated sample (Table S1). The average C_Q value of local disordered Mg centers in the activated sample (9.7 MHz) is also significantly larger than those in the guest-loaded samples (4.8–5.0 MHz). In summary, the spectra of all the guest-loaded forms are similar as a result of 6-coordinate Mg while the spectrum of the activated form is distinct due to 5-coordinate Mg.

The static and MAS ^{25}Mg SSNMR data allow us to develop a more detailed understanding of the MOF structure. The perfectly ordered Mg centers exhibit a single second-order quadrupolar powder pattern for all Mg$_2$(dobpdc) samples, suggesting they belong to the same crystallographic Mg site. However, a portion of Mg centers that belong to this crystallographic Mg site experience significant local disorder, yielding a distribution of quadrupolar coupling interactions and the featureless and asymmetric line shape. The average quadrupolar coupling of local disordered Mg centers, described by the C_Q value shown in the Czjzek distribution, is close to the C_Q value of the perfect ordered Mg centers. The observation of a single powder pattern for perfectly ordered Mg

centers agrees well with the proposed trigonal space group $P3_121$ (No. 152) as its more crystalline analog Mn_2(dobpdc). The DFT-calculated structures, however, have a space group of P_1 (No. 1, a subgroup of $P3_121$) with six crystallographically distinct Mg sites.[15] The reduction of crystal symmetry results from the fact that there is no disorder allowed for both framework and guest molecules when conducting DFT calculations. The structure of the activated sample was also calculated as P_1 for comparison purposes, yet its geometry is very close to the $P3_121$ structure. The similarity between the experimental and calculated C_Q values of both the activated sample (8.5 vs. 10.4 MHz) and the mmen-loaded sample (6.3 vs. 7.4 MHz) indicates that the actual geometry of the Mg coordination sphere is close to the calculated geometry, which is a square pyramid for the activated sample and a distorted octahedron for the mmen-loaded sample.
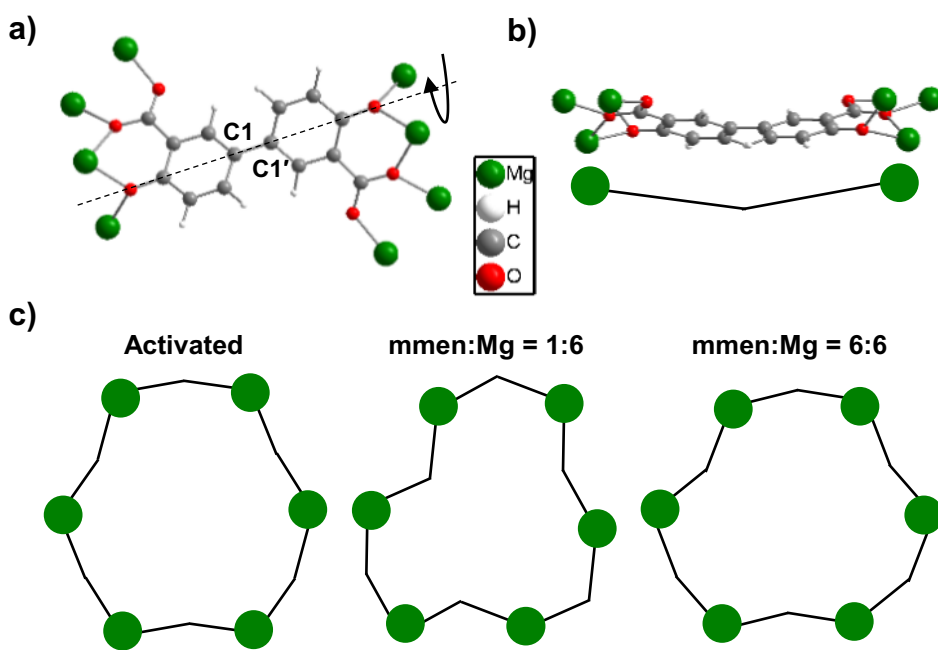

Figure 6. The dobpdc[4-] linker viewed perpendicular (a) or parallel (b) to the channels. Schematic illustration of the channels of various Mg_2(dobpdc) samples (c). The green circles represent the Mg^{2+} helix, while the bent solid lines represent the dobpdc[4-] linkers. The distortion degree of the MOF channels is exaggerated to illustrate the framework deformation.

The flexibility of dobpdc[4-] linkers plays a critical role in the local disorder of Mg centers for various Mg$_2$(dobpdc) samples. As Figure 6 shows, the dobpdc[4-] linker has an internal rotational degree of freedom along the C1–C1′ bond. As a result, the two rings of its biphenyl unit are typically not co-planar, inducing an apparent "bending" of the dobpdc[4-] linker if viewed along the channels. DFT calculations indicate the degree of "bending" varies in different Mg$_2$(dobpdc) samples (*e.g.,* the activated sample and the mmen-loaded samples with different mmen loading levels), inducing different distortion degrees for the channels (Figure 6c and S2).[15] A recent paper also predicts the framework deformation for a MOF with the same topology but longer linkers (five benzene rings) induced by adsorbed Ar.[51] The heterogeneous distribution of guest molecules can therefore yield a distribution of distortion degrees for different channels as well as the local disorder at Mg centers. Molecular dynamic (MD) simulations (Figure 7 and the movie in Supporting Information) reveal that the mmen molecules are moving within the MOF channels. The dynamic framework deformation associated with the diamine motions makes local Mg environments more disordered and generates a fluctuating local EFG around [25]Mg nucleus, efficiently accelerating the spin-lattice relaxation of [25]Mg. The motions of other guest molecules such as DMF, methanol, and H$_2$O, should have similar consequences. Taken together, the MD and DFT calculations validate that such framework deformation can lead to large distributions in the [25]Mg NMR parameters (Table S2).
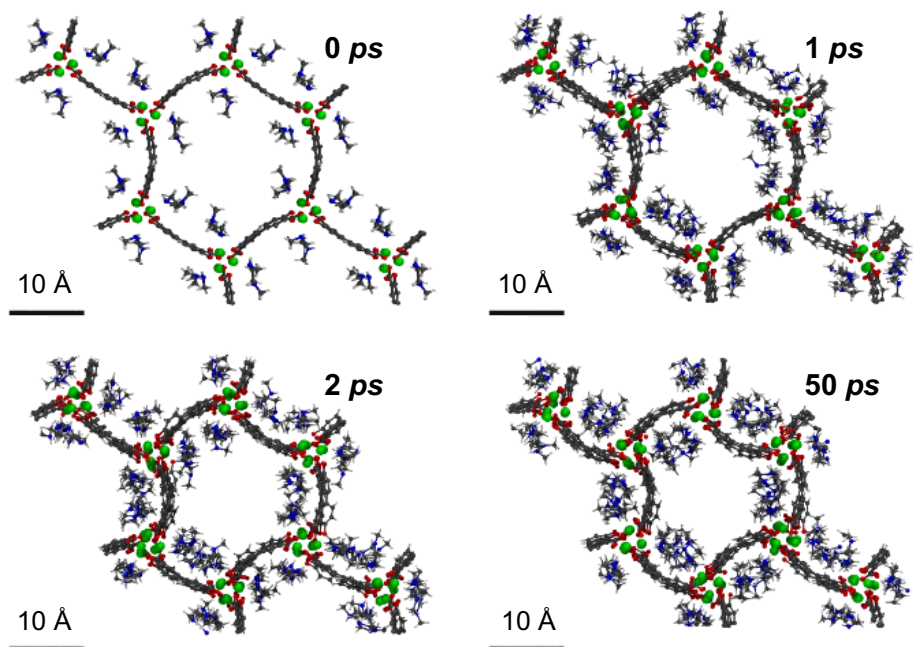
Figure 7. Snapshots of MD simulations for mmen-Mg$_2$(dobpdc) (mmen : Mg = 6 : 6) as a function of evolution time. Green, grey, red, blue and white spheres represent Mg, C, O, N and H atoms, respectively.

The DMF-loaded Mg$_2$(dobpdc) was crystallized directly from the reaction mixture thus the distribution of DMF within the MOF channels is relatively homogenous, giving rise to the highest crystallinity, consistent with the observed small fraction of local disordered Mg centers. The activated form was prepared by heating the methanol-exchanged sample under dynamic vacuum. Disorder in the local Mg environment increases due to the non-uniform release of the methanol molecules that bind to the Mg sites, which causes the internal rotational degree of the dobpdc^{4-} linker to vary from site to site during the activation process. In principle, the activation-induced disorder should eventually recover to the perfectly ordered state (*i.e.*, global energy minimum). However, the reorganization of the local environment of a Mg center requires the simultaneous reformation of the local environments of many other Mg centers in this MOF. As a result these disordered regions are likely to stay at the local energy minima even after the activation process.

The fraction of Mg centers with local disorder increases significantly in the H_2O- or mmen-loaded samples because they were prepared by soaking the activated form of $Mg_2(dobpdc)$ in H_2O or mmen solution (in toluene). The distribution of H_2O or mmen within the channels is therefore not as homogeneous as DMF, confirmed by the larger fraction of locally disordered Mg centers in the former samples. An extended ^{15}N SSNMR study is currently underway in our laboratory to try to understand the relationship of mmen and other diamine adsorbate molecular dynamics to the framework deformation.

Conclusions

In the current work, ^{25}Mg SSNMR spectra have uncovered the local Mg environments within variants of the MOF $Mg_2(dobpdc)$ and unambiguously probed the conversion between five-coordinate Mg in the activated sample and six-coordinate Mg in the solvent- or diamine-loaded samples. Decent agreement between experiment and DFT calculations confirms the types of Mg coordination environments. NMR results also show that the local environments of a significant amount of Mg centers are disordered. MD and DFT calculations indicate the local disorder is due to the framework deformation accompanied by the guest distributions and dynamics.

ASSOCIATED CONTENT

Supporting Information. Experimental details including powder XRD patterns, theoretical calculations, NMR theory of quadrupolar nucleus and Czjzek distribution, and additional NMR spectra and analyses. Movie of dynamic framework deformation.

The following files are available free of charge via the Internet at http://pubs.acs.org.

AUTHOR INFORMATION

Corresponding Author

*Email: qidongxujun@gmail.com.

Notes

The authors declare no competing financial interests.

REFERENCES

(1) IPCC. Contributions of Working Group I to the Fifth Assessment Report of the Intergovernmental Panel on Climate Change. In *Climate Change 2013: The Physical Science Basis*; Stocker, T. F., Qin, D., Plattner, G.-K., Tignor, M. M. B., Allen, S. K., Boschung, J., Nauels, A., Xia, Y., Bex, V., Midgley, P. M., Eds.; Cambridge University Press: Cambridge, United Kingdom and New York, 2013.

(2) Orr, J. C.; Fabry, V. J.; Aumont, O.; Bopp, L.; Doney, S. C.; Feely, R. A.; Gnanadesikan, A.; Gruber, N.; Ishida, A.; Joos, F. *et al*. Anthropogenic Ocean Acidification Over the Twenty-First Century and Its Impact on Calcifying Organisms. *Nature* **2005**, *437*, 681-686.

(3) IPCC *IPCC Special Report on Carbon Dioxide Capture and Storage*, Cambridge University Press: Cambridge, United Kingdom and New York, 2005.

(4) Davis, S. J.; Caldeira, K.; Matthews, H. D. Future CO_2 Emissions and Climate Change from Existing Energy Infrastructure. *Science* **2010**, *329*, 1330-1333.

(5) Bhown, A. S.; Freeman, B. C. Analysis and Status of Post-Combustion Carbon Dioxide Capture Technologies. *Environ. Sci. Technol.* **2011**, *45*, 8624-8632.

(6) Smit, B.; Reimer, J. A.; Oldenburg, C. M.; Bourg, I. C. *Introduction to Carbon Capture and Sequestration*, Imperial College Press: London, United Kingdom, 2014.

(7) Choi, S.; Drese, J. H.; Jones, C. W. Adsorbent Materials for Carbon Dioxide Capture from Large Anthropogenic Point Sources. *ChemSusChem* **2009**, *2*, 796-854.

(8) Sumida, K.; Rogow, D. L.; Mason, J. A.; McDonald, T. M.; Bloch, E. D.; Herm, Z. R.; Bae, T.-H.; Long, J. R. Carbon Dioxide Capture in Metal–Organic Frameworks. *Chem. Rev.* **2012**, *112*, 724-781.

(9) Zeng, Y.; Zou, R.; Zhao, Y. Covalent Organic Frameworks for CO_2 Capture. *Adv. Mater.* **2016**, *28*, 2855-2873.

(10) Wu, H.; Simmons, J. M.; Srinivas, G.; Zhou, W.; Yildirim, T. Adsorption Sites and Binding Nature of CO_2 in Prototypical Metal–Organic Frameworks: A Combined Neutron Diffraction and First-Principles Study. *J. Phys. Chem. Lett.* **2010**, *1*, 1946-1951.

(11) Kong, X.; Scott, E.; Ding, W.; Mason, J. A.; Long, J. R.; Reimer, J. A. CO_2 Dynamics in a Metal–Organic Framework with Open Metal Sites. *J. Am. Chem. Soc.* **2012**, *134*, 14341-14344.

(12) Lin, L.-C.; Kim, J.; Kong, X.; Scott, E.; McDonald, T. M.; Long, J. R.; Reimer, J. A.; Smit, B. Understanding CO_2 Dynamics in Metal–Organic Frameworks with Open Metal Sites. *Angew. Chem. Int. Ed.* **2013**, *52*, 4410-4413.

(13) Wang, W. D.; Lucier, B. E. G.; Terskikh, V. V.; Wang, W.; Huang, Y. Wobbling and Hopping: Studying Dynamics of CO_2 Adsorbed in Metal–Organic Frameworks via ^{17}O Solid-State NMR. *J. Phys. Chem. Lett.* **2014**, *5*, 3360-3365.

(14) McDonald, T. M.; Mason, J. A.; Kong, X.; Bloch, E. D.; Gygi, D.; Dani, A.; Crocella, V.; Giordanino, F.; Odoh, S. O.; Drisdell, W. S. *et al*. Cooperative Insertion of CO_2 in Diamine-Appended Metal-Organic Frameworks. *Nature* **2015**, *519*, 303-308.

(15) Vlaisavljevich, B.; Odoh, S. O.; Schnell, S.; Dzubak, A. L.; Lee, K.; Planas, N.; Neaton, J.; Gagliardi, L.; Smit, B. CO_2 Induced Phase Transitions in Diamine-Appended Metal Organic Frameworks. *Chem. Sci.* **2015**, *6*, 5177-5185.

(16) Kroeker, S.; Stebbins, J. F. Magnesium Coordination Environments in Glasses and Minerals: New Insight from High-Field Magnesium-25 MAS NMR. *Am. Mineral.* **2000**, *85*, 1459-1464.

(17) Hung, I.; Schurko, R. W. Solid-State [25]Mg QCPMG NMR of Bis(cyclopentadienyl)magnesium. *Solid State Nucl. Magn. Reson.* **2003**, *24*, 78-93.

(18) Wong, A.; Ida, R.; Mo, X.; Gan, Z.; Poh, J.; Wu, G. Solid-State ^{25}Mg NMR Spectroscopic and Computational Studies of Organic Compounds. Square-Pyramidal Magnesium(II) Ions in Aqua(magnesium) Phthalocyanine and Chlorophyll a. *J. Phys. Chem. A* **2006**, *110*, 10084-10090.

(19) Widdifield, C. M.; Bryce, D. L. Crystallographic Structure Refinement with Quadrupolar Nuclei: A Combined Solid-State NMR and GIPAW DFT Example Using MgBr$_2$. *Phys. Chem. Chem. Phys.* **2009**, *11*, 7120-7122.

(20) Davis, M. C.; Brouwer, W. J.; Wesolowski, D. J.; Anovitz, L. M.; Lipton, A. S.; Mueller, K. T. Magnesium Silicate Dissolution Investigated by ^{29}Si MAS, ^{1}H-^{29}Si CPMAS, ^{25}Mg QCPMG, and ^{1}H-^{25}Mg CP QCPMG NMR. *Phys. Chem. Chem. Phys.* **2009**, *11*, 7013-7021.

(21) Sideris, P. J.; Nielsen, U. G.; Gan, Z.; Grey, C. P. Mg/Al Ordering in Layered Double Hydroxides Revealed by Multinuclear NMR Spectroscopy. *Science* **2008**, *321*, 113-117.

(22) Pallister, P. J.; Moudrakovski, I. L.; Ripmeester, J. A. Mg-25 Ultra-High Field Solid State NMR Spectroscopy and First Principles Calculations of Magnesium Compounds. *Phys. Chem. Chem. Phys.* **2009**, *11*, 11487-11500.

(23) Cahill, L. S.; Hanna, J. V.; Wong, A.; Freitas, J. C. C.; Yates, J. R.; Harris, R. K.; Smith, M. E. Natural Abundance ^{25}Mg Solid-State NMR of Mg Oxyanion Systems: A Combined Experimental and Computational Study. *Chem. –Eur. J.* **2009**, *15*, 9785-9798.

(24) Griffin, J. M.; Berry, A. J.; Ashbrook, S. E. Observation of "Hidden" Magnesium: First-Principles Calculations and ^{25}Mg Solid-State NMR of Enstatite. *Solid State Nucl. Magn. Reson.* **2011**, *40*, 91-99.

(25) Laurencin, D.; Gervais, C.; Stork, H.; Kramer, S.; Massiot, D.; Fayon, F. ^{25}Mg Solid-State NMR of Magnesium Phosphates: High Magnetic Field Experiments and Density Functional Theory Calculations. *J. Phys. Chem. C* **2012**, *116*, 19984-19995.

(26) Mali, G.; Trebosc, J.; Martineau, C.; Mazaj, M. Structural Study of Mg-Based Metal–Organic Frameworks by X-ray Diffraction, ^{1}H, ^{13}C, and ^{25}Mg Solid-State NMR Spectroscopy, and First-Principles Calculations. *J. Phys. Chem. C* **2015**, *119*, 7831-7841.

(27) Xu, J.; Terskikh, V. V.; Huang, Y. Resolving Multiple Non-equivalent Metal Sites in Magnesium-Containing Metal–Organic Frameworks by Natural Abundance ^{25}Mg Solid-State NMR Spectroscopy. *Chem. –Eur. J.* **2013**, *19*, 4432-4436.

(28) Xu, J.; Terskikh, V. V.; Huang, Y. ^{25}Mg Solid-State NMR: A Sensitive Probe of Adsorbing Guest Molecules on a Metal Center in Metal–Organic Framework CPO-27-Mg. *J. Phys. Chem. Lett.* **2013**, *4*, 7-11.

(29) Siegelman, R. L.; McDonald, T. M.; Gonzalez, M. I.; Martell, J.; Milner, P. J.; Mason, J. A.; Berger, A. H.; Bhown, A. S.; Long, J. R. Controlling Cooperative CO$_2$ Adsorption in Diamine-Appended Mg$_2$(dobpdc) Metal–Organic Frameworks. *J. Am. Chem. Soc.* **2017**, doi: 10.1021/jacs.7b05858.

(30) Larsen, F. H.; Jakobsen, H. J.; Ellis, P. D.; Nielsen, N. C. Sensitivity-Enhanced Quadrupolar-Echo NMR of Half-Integer Quadrupolar Nuclei. Magnitudes and Relative Orientation of Chemical Shielding and Quadrupolar Coupling Tensors. *J. Phys. Chem. A* **1997**, *101*, 8597-8606.

(31) Kunwar, A. C.; Turner, G. L.; Oldfield, E. Solid-State Spin-Echo Fourier Transform NMR of ^{39}K and ^{67}Zn Salts at High Field. *J. Magn. Reson.* **1986**, *69*, 124-127.

(32) Iuga, D.; Schäfer, H.; Verhagen, R.; Kentgens, A. P. M. Population and Coherence Transfer Induced by Double Frequency Sweeps in Half-Integer Quadrupolar Spin Systems. *J. Magn. Reson.* **2000**, *147*, 192-209.

(33) Bennett, A. E.; Rienstra, C. M.; Auger, M.; Lakshmi, K. V.; Griffin, R. G. Heteronuclear Decoupling in Rotating Solids. *J. Chem. Phys.* **1995**, *103*, 6951-6958.

(34) Goswami, M.; van Bentum, P. J. M.; Kentgens, A. P. M. Sensitivity Enhancement in MAS NMR of Half-Integer Quadrupolar Nuclei Using Sideband Selective Double-Frequency Sweeps. *Can. J. Chem.* **2011**, *89*, 1130-1137.

(35) Goswami, M.; van Bentum, P. J. M.; Kentgens, A. P. M. Repetitive Sideband-Selective Double Frequency Sweeps for Sensitivity Enhancement of MAS NMR of Half-Integer Quadrupolar Nuclei. *J. Magn. Reson.* **2012**, *219*, 25-32.

(36) Massiot, D.; Fayon, F.; Capron, M.; King, I.; Le Calve, S.; Alonso, B.; Durand, J.-O.; Bujoli, B.; Gan, Z.; Hoatson, G. Modeling One- and Two-Dimensional Solid-State NMR Spectra. *Magn. Reson. Chem.* **2002**, *40*, 70-76.

(37) Czjzek, G.; Fink, J.; Götz, F.; Schmidt, H.; Coey, J. M. D.; Rebouillat, J. P.; Liénard, A. Atomic Coordination and the Distribution of Electric Field Gradients in Amorphous Solids. *Phys. Rev. B* **1981**, *23*, 2513-2530.

(38) Neuville, D. R.; Cormier, L.; Massiot, D. Al Environment in Tectosilicate and Peraluminous Glasses: A ^{27}Al MQ-MAS NMR, Raman, and XANES Investigation. *Geochim. Cosmochim. Acta* **2004**, *68*, 5071-5079.

(39) Valiev, M.; Bylaska, E. J.; Govind, N.; Kowalski, K.; Straatsma, T. P.; Van Dam, H. J. J.; Wang, D.; Nieplocha, J.; Apra, E.; Windus, T. L. *et al.* NWChem: A Comprehensive and Scalable Open-Source Solution for Large Scale Molecular Simulations. *Comput. Phys. Commun.* **2010**, *181*, 1477-1489.

(40) Plimpton, S. Fast Parallel Algorithms for Short-Range Molecular Dynamics. *J. Comput. Phys.* **1995**, *117*, 1-19.

(41) van Duin, A. C. T.; Dasgupta, S.; Lorant, F.; Goddard, W. A. ReaxFF: A Reactive Force Field for Hydrocarbons. *J. Phys. Chem. A* **2001**, *105*, 9396-9409.

(42) Aktulga, H. M.; Fogarty, J. C.; Pandit, S. A.; Grama, A. Y. Parallel Reactive Molecular Dynamics: Numerical Methods and Algorithmic Techniques. *Parallel Computing* **2012**, *38*, 245-259.

(43) Huang, L.; Joshi, K. L.; Duin, A. C. T. v.; Bandosz, T. J.; Gubbins, K. E. ReaxFF Molecular Dynamics Simulation of Thermal Stability of a $Cu_3(BTC)_2$ Metal-Organic Framework. *Phys. Chem. Chem. Phys.* **2012**, *14*, 11327-11332.

(44) Cheung, S.; Deng, W.-Q.; van Duin, A. C. T.; Goddard, W. A. ReaxFFMgH Reactive Force Field for Magnesium Hydride Systems. *J. Phys. Chem. A* **2005**, *109*, 851-859.

(45) Kentgens, A. P. M.; Verhagen, R. Advantages of Double Frequency Sweeps in Static, MAS and MQMAS NMR of Spin *I*=3/2 Nuclei. *Chem. Phys. Lett.* **1999**, *300*, 435-443.

(46) Xu, J.; Lucier, B. E. G.; Lin, Z.; Sutrisno, A.; Terskikh, V. V.; Huang, Y. New Insights into the Short-Range Structures of Microporous Titanosilicates As Revealed by [47/49]Ti, [23]Na, [39]K, and ^{29}Si Solid-State NMR Spectroscopy. *J. Phys. Chem. C* **2014**, *118*, 27353-27365.

(47) Sutrisno, A.; Liu, L.; Xu, J.; Huang, Y. Natural Abundance Solid-State [67]Zn NMR Characterization of Microporous Zinc Phosphites and Zinc Phosphates at Ultrahigh Magnetic Field. *Phys. Chem. Chem. Phys.* **2011**, *13*, 16606-16617.

(48) Hung, I.; Gan, Z. On the Practical Aspects of Recording Wideline QCPMG NMR Spectra. *J. Magn. Reson.* **2010**, *204*, 256-265.

(49) Ernst, H.; Freude, D.; Wolf, I. Multinuclear Solid-State NMR Studies of Broensted Sites in Zeolites. *Chem. Phys. Lett.* **1993**, *212*, 588-596.

(50) Eckert, H. Structural Characterization of Noncrystalline Solids and Glasses Using Solid State NMR. *Prog. Nucl. Magn. Reson. Spectrosc.* **1992**, *24*, 159-293.

(51) Jawahery, S.; Simon, C. M.; Braun, E.; Witman, M.; Tiana, D.; Vlaisavljevich, B.; Smit, B. Adsorbate-Induced Lattice Deformation in IRMOF-74 Series. *Nature Commun.* **2017**, *8*, 13945.

TOC GRAPHICS

^{25}Mg NMR   **MOF**